

Passivation Behavior of Al₈₈Fe₆La₆ Glassy Alloy in NaOH and H₂SO₄ Solutions

R. Li¹, X.Y. Li^{2*}, J. Pang², L.J. Yin², H.D. Zhang¹, C.D. Cao³, W.M. Wang^{1*}

¹Key Laboratory for Liquid-Solid Structural Evolution and Processing of Materials (Ministry of Education), Shandong University, Jinan 250061, China

²Qingdao Yunlu Energy Technology Co., Ltd, Qingdao 266109, China

³Department of applied physics, Northwest Polytechny University, Xian 710072, China

*E-mail: weiminw@sdu.edu.cn; fj-kaifa@yunlu.com.cn

Received: 23 December 2012 / Accepted: 17 January 2013 / Published: 1 February 2013

The passivation behavior of Al₈₈Fe₆La₆ glassy ribbons in NaOH and H₂SO₄ solutions has been studied in this paper. The anodic polarization shows a good passivation up to the measurement limit, which can be ascribed to the heterogeneity in micro- and nano- scales, providing the bridges to transport the Fe atoms into the oxide film. After anodic polarization, the cracks appeared in the surface of ribbon can be divided into A and B types. The mechanism of crack formation is discussed in this study and possibly used in the powder manufacturing technology.

Keywords: amorphous materials; corrosion; crack; electron microscopy

1. INTRODUCTION

Since last decades, the amorphous alloys such as Al-TM-RE-based alloys have been found to have an excellent corrosion resistance due to their chemical and structural homogeneity [1]. The amorphous Al-Co-Ca alloy can act as an effective corrosion inhibitor to Aluminum alloy, which improves the pitting potential E_{pit} of Al-based alloys drastically [2]. Rare earth elements also act as a corrosion inhibitor [3]. According to our earlier works, we found that 1 at% Fe addition to substitute Ni in Al₈₄Ni₁₀La₆ amorphous alloy would enhance the alloy's corrosion resistance [4]. However, to authors' knowledge, there is no work on the corrosion resistance of Al-Fe-La glasses in which Ni is replaced by Fe completely.

Unlike $\text{Al}_{86}\text{Ni}_6\text{La}_6\text{Cu}_2$ amorphous alloy [5], the nanocrystalline phase in some amorphous matrix can improve the corrosion resistance. The work of Alvarez et al shows that the crystalline Ni-B-Sn alloy has a better corrosion resistance than the amorphous counterpart because of the precipitation of Ni and Ni_3B phases [6]. In case of nanocrystalline/amorphous FeCuNbSiB composites, the superficial SiO_2 film is easily formed and improves the alloy's corrosion resistance [7]. The excellent corrosion resistance of the nanocrystalline/amorphous composites is explained by the oxide bridging model [8,9], which assume that the interface acts as a bridge to transport the protective elements to the oxide film.

Besides annealing the glassy precursor, adjusting the cooling rate is another measure to obtain the nanocrystalline/amorphous composites [10]. Cooling rate has a strong effect on the microstructure and mechanical properties of rapidly solidified Al-based bulk alloys [11]. Generally, increasing the cooling rate can optimize the micro-structure of amorphous alloys and improve their properties. However, there were little studies on the correlation between the cooling rate and the corrosion resistance of Al-based alloys. In this paper, we set the $\text{Al}_{88}\text{Fe}_6\text{La}_6$ alloy as starting alloy, spun the melt with different cooling rates, investigated the corrosion behavior of the alloy in different solutions, and discussed the inherent mechanism of the passivation and crack formation during the anodic polarization.

2. EXPERIMENTAL

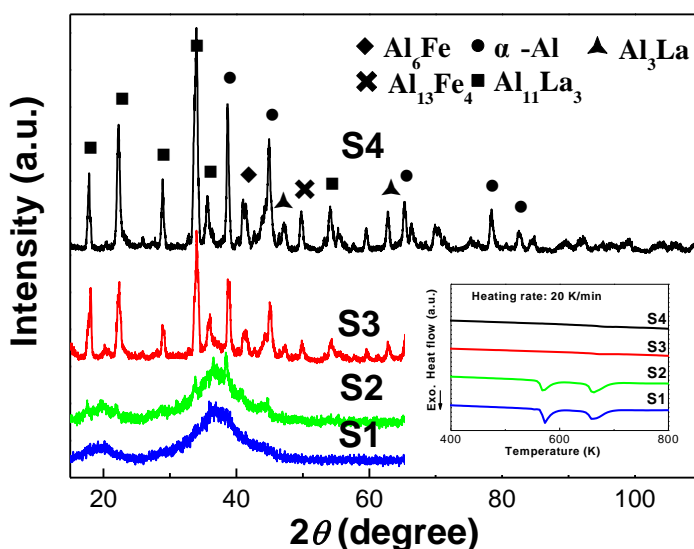


Figure 1. XRD patterns of $\text{Al}_{88}\text{Fe}_6\text{La}_6$ ribbons at different circumferential speeds R_c : 22.0 m/s (S1), 14.7 m/s (S2), 11.0m/s (S3) and 7.3m/s (S4). The inset shows the DSC scans of $\text{Al}_{88}\text{Fe}_6\text{La}_6$ ribbons at different circumferential speeds.

In this study, the ingot of $\text{Al}_{88}\text{Fe}_6\text{La}_6$ was obtained by induction-melting the mixture of pure raw materials such as Al (99.9 % mass percent), Fe (99.7 % mass percent) and La (99.5 % mass percent). The ribbons were prepared by a single roller melt-spinning with the different circumferential speeds R_c : 22.0 m/s (labeled as S1), 14.7 m/s (labeled as S2), 11.0 m/s (labeled as S3), and 7.3 m/s (labeled as S4).

The X-ray diffraction (XRD) patterns of ribbons with various R_c are shown in Fig. 1, which are obtained by a D/Max-rB diffractometer with Cu $K\alpha$ radiation. It can be seen that the S1 and S2 ribbons exhibit two broad diffraction peaks centered at $2\theta = 18 \sim 20$ deg and $2\theta = 36 \sim 38$ deg. There are several crystalline peaks embedded in the XRD pattern of S2. And no broad diffraction peak exists in curves of S3 and S4. Using peak decomposing, the volume fraction of the amorphous phase (f_a) of S1, S2, S3 and S4 are 100 %, 93 %, 0, and 0, respectively. In addition, with decreasing R_c , α -Al and $\text{Al}_{11}\text{La}_3$ precipitated firstly, and then the Al-Fe intermetallic phases, such as Al_5Fe_2 and $\text{Al}_{13}\text{Fe}_4$, formed in the samples. The thermal behavior of samples was examined using a differential scanning calorimetry (Netzsch DSC 404c) at a heating rate of 20 K/min, which is shown in the inset of Fig. 1. There are two exothermic peaks in the curves of S1 and S2, indicating two steps in crystallization process. Combining present XRD patterns and earlier DSC curves of other Al-TM-RE glasses [12], the first crystallization process of S1 and S2 is precipitating out not only α -Al, but also intermetallics. There is no exothermic peak in DSC curves of S3 and S4 curves, agreeing with the corresponding XRD patterns.

The polarization curves of samples were measured by a LK 2005A electrochemical workstation. The electrolytes were H_2SO_4 and NaOH solutions with contents of 0.1, 0.5, 1.0 M, and the corresponding reference electrodes were Hg| Hg_2SO_4 ($c_{\text{SO}_4^-} = 0.62$ M) and Hg| HgO ($c_{\text{OH}^-} = 1$ M), respectively. All polarization curves were obtained at the room temperature with a scanning rate of 5 mV/s.

Microstructure investigation and phase identification were carried out using TECNAI F30 G^2 transmission electronic microscopy (TEM) (FEI, USA). The surface morphologies and local compositions of as-spun and polarized samples were studied by scanning electron microscopy (SEM, HITACHI SU70).

3. RESULTS

The polarization curves of samples with various R_c in 0.1 M NaOH and H_2SO_4 solutions are shown in Fig. 2. In NaOH solution, all ribbons exhibit a stable passivation (Fig. 2a), and no drastic current increment appears even until the limit of the measuring range (10 V). But a drastic current increment happens in the curve of $\text{Al}_{88}\text{Ni}_6\text{Gd}_6$ glassy ribbon [13]. There was no drastic current increment in H_2SO_4 solution either (Fig. 2b). This phenomenon was also found in amorphous and nanoquasicrystalline Zr-Pd and Zr-Pt alloys [14], but not met in most glasses such as Al-Ni-La glasses

[4], Fe-Si-B glasses [15] and Mg-based glass [16]. For comparison, the polarization curve of pure Al ribbon with $R_c = 22.0$ m/s in 0.1 M NaOH solution is shown in Fig. 2a. Obviously, the corrosion potential of $\text{Al}_{88}\text{Fe}_6\text{La}_6$ is higher than pure Al, while the corrosion current density is lower, indicating that the $\text{Al}_{88}\text{Fe}_6\text{La}_6$ ribbon has a very good corrosion resistance. This phenomenon is consistent with the Al-Cu system [17]. In addition, the corrosion current density (I_{corr}) of ribbons increases with decreasing R_c in NaOH and H_2SO_4 solutions, indicating that the corrosion resistance of ribbons is getting worse with reducing R_c .

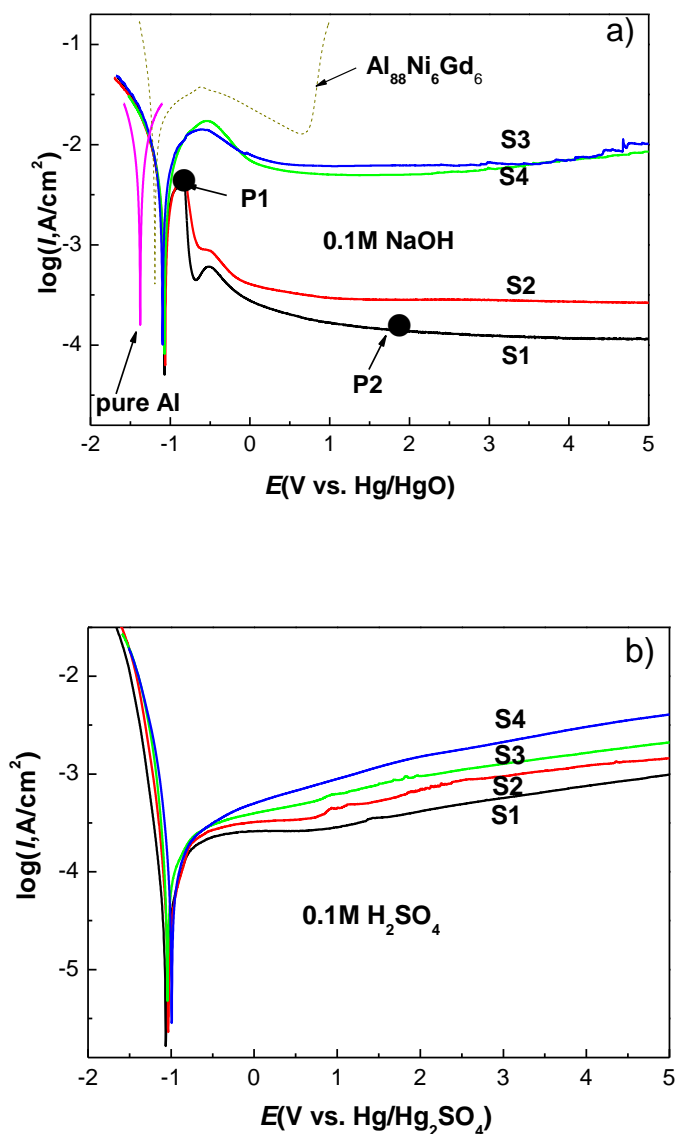


Figure 2. Potentiodynamic polarization curves of $\text{Al}_{88}\text{Fe}_6\text{La}_6$ ribbons at different circumferential speeds R_c : 22.0 m/s (S1), 14.7 m/s (S2), 11.0m/s (S3) and 7.3m/s (S4). a) 0.1 M NaOH; b) 0.1 M H_2SO_4 . The curve of $\text{Al}_{88}\text{Ni}_6\text{Gd}_6$ glassy ribbon is cited from [13]

To explore the corrosion phenomenon happened for samples in acid and alkaline solutions, we improved the contents of electrolytes to 0.5 and 1.0 M. Fig. 3 shows the polarization curves of S1 ribbons in 0.1, 0.5 and 1.0 M NaOH solutions. The polarization curves in H_2SO_4 solution are not shown in here. Obviously, there is no drastic increase of current in the higher concentration solutions, indicating that the phenomenon is stable and repeatable. With increasing the content, the current density in passive region I_{pass} increases significantly. Moreover, under the low content condition, the content's effect on I_{pass} is greater than that under the high content condition, indicating a saturation phenomenon of I_{pass} during increasing the solution's content.

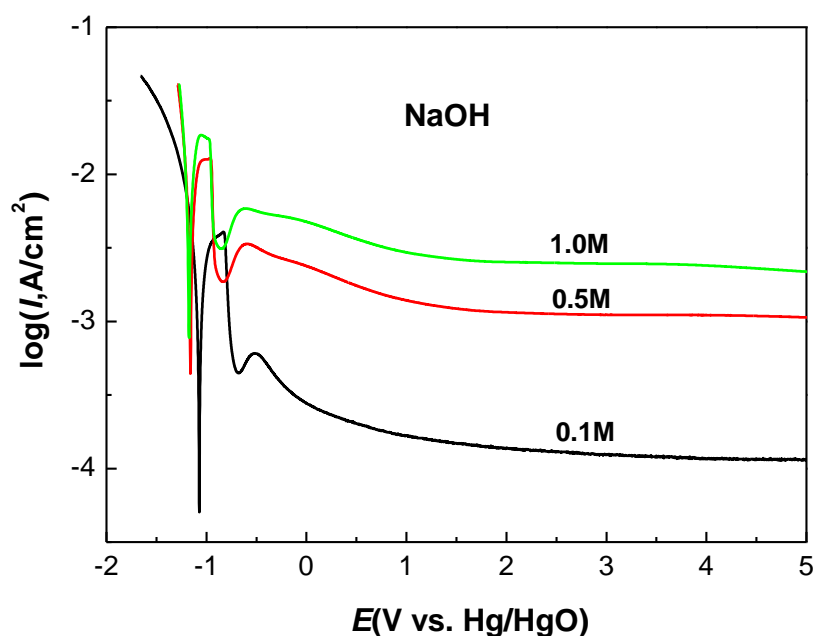


Figure 3. Potentiodynamic polarization curves of $Al_{88}Fe_6La_6$ ribbons with circumferential speed $R_c = 22.0$ m/s (S1) in 0.1, 0.5 and 1.0 M NaOH solutions.

To further analyze the corrosion process, we stopped the anodic polarization of the ribbons with $R_c = 22.0$ m/s in 0.1 M NaOH solution at P1 and P2 points in Fig. 2a. The scanning electron microscopy (SEM) photographs of as-cast, polarized ribbons until P1 and P2 are shown in Fig. 4. The contents of Al, Fe, La and O obtained by the energy dispersive spectroscopy (EDS) are listed in Table 1. From the morphology of the points for spectrums 3, 4, 5 and 6, little surface contamination is found in the investigated range. In the wheel surface (dark surface) of ribbons, some intermetallic phases in size of $2 \mu m$ are embedded on the amorphous matrix (Fig. 4 a). The enlarged photograph shows that the intermetallic phases include three types: the dendrite phase outside, the block one in the core, and the flower-like in the middle (Fig. 4 b). According to the XRD results (Fig. 1) and non-faceted crystallization mechanism [18], the dendrite phase can be indentified as fcc-Al. On basis of the EDS

results (Table 1), the block one is Fe-Al compound. And the flower-like one is Al-La compound as indicated by lining scanning of EDS (not shown here).

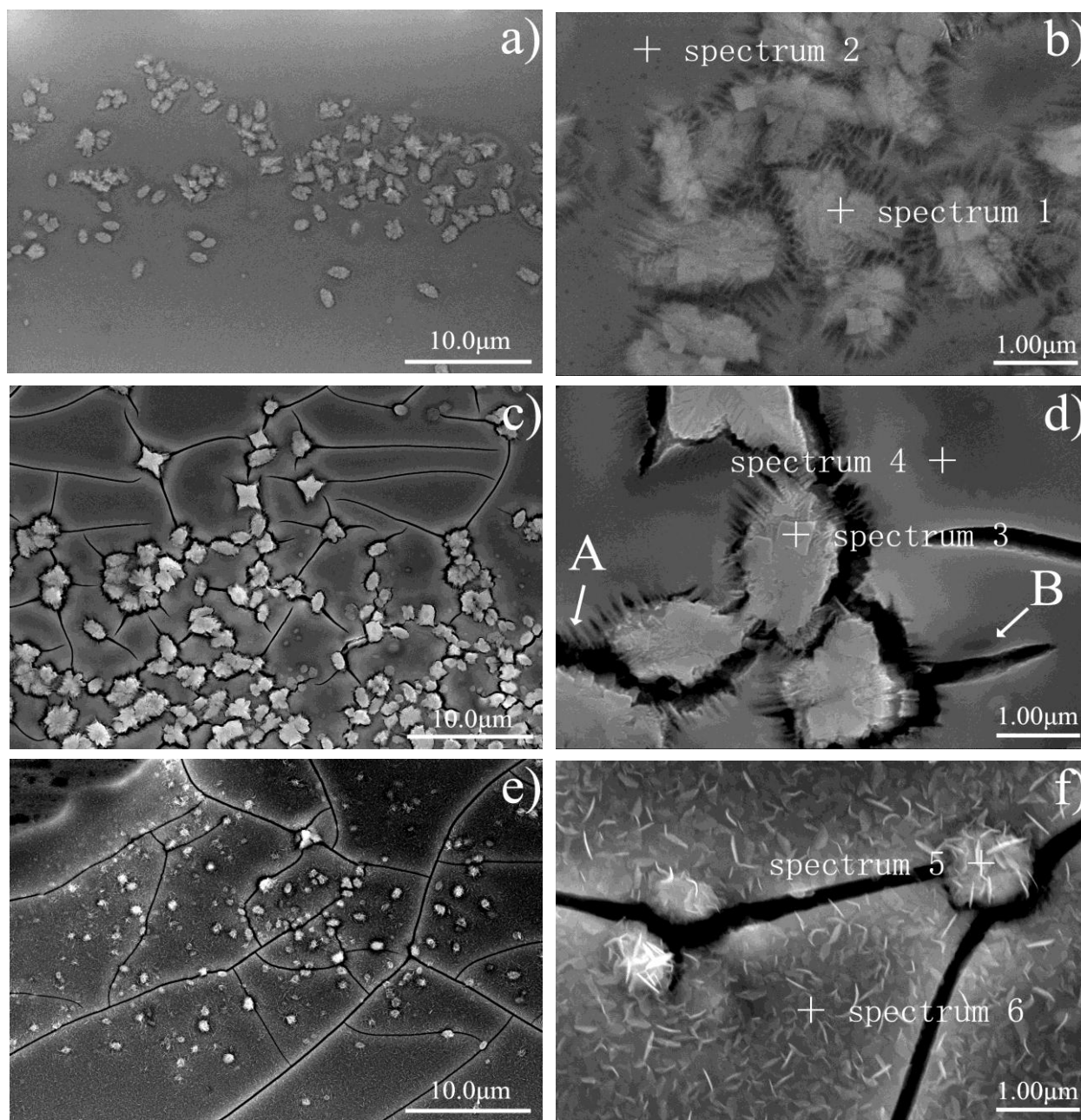


Figure 4. The SEM photographs of wheel-side surface of ribbons with $R_c = 22.0$ m/s (S1). a) and b) as-spun; c) and d) anodically polarized in 0.1 M NaOH until -0.85 V vs. Hg/HgO (P1); and e) and f) anodically polarized in 0.1 M NaOH until 1.75 V vs. Hg/HgO (P2). + denotes the positions of EDS. A and B denote cracks.

Table 1. The energy dispersive spectroscopy (EDS) contents of Al, Fe, La and O of as-spun, anodically polarized Al₈₈Fe₆La₆ samples (S1) until P1 and P2 points denoted in Fig. 2.

	positions	Al (at.%)	Fe (at.%)	La (at.%)	O (at.%)
As-spun	Spectrum 1	84.6	9.3	6.1	-
	Spectrum 2	87.0	6.5	6.5	-
P1	Spectrum 3	14.5	16.8	11.0	57.7
	Spectrum 4	16.8	11.1	10.1	62.0
P2	Spectrum 5	19.6	10.5	8.9	61.0
	Spectrum 6	25.9	7.8	6.3	60.0

EDS Positions are shown in Fig. 4

After the anodic polarization until P1, i.e., just before passivation, the dendrite Al phase dissolves firstly, leaving the trenches in the ribbons (Fig. 4 c and d). Cracks (A denoted in Fig. 4 d) initiate from these trenches and propagate along the intermetallic/matrix interface, resulting in the separation of crystal phases from the amorphous matrix. Meanwhile, the A cracks have some sharp edges and help the cracks (B denoted in Fig. 4 d) to propagate towards the amorphous matrix. Here, crack A is rough, depending on the outline of intermetallic phases, but crack B is smooth and almost linear. After a further passivation until P2, the B cracks extend and form a network (Fig. 4 e). Meanwhile, a layer of corrosion products are covered on the matrix without any pits (Fig. 4 f). According to the EDS data in Table 1, the oxygen content of samples rises firstly and then keeps stable with increasing the polarization voltage, indicating that the oxide film is formed rapidly and very stable.

4. DISCUSSION

4.1 Micro-structural heterogeneity in the Al-Fe-La glassy alloys

As shown in the XRD patterns (Fig. 1), the position 2θ of (111) peak/plane of Al phase in the samples varies with R_c , resulting in the change of (111) plane spacing d according to the Bragg equation [19]. The position 2θ of (111) plane of Al, its spacing d and the volume fraction of amorphous phase f_a in the samples are listed in Table 2. With decreasing R_c , the measured d of (111)_{Al} decreases, and is lower than that of pure Al (0.23381 nm [20]). Since the atomic radius of Al, Fe and La are 0.143, 0.127 and 0.187 nm, respectively, it should be Fe atoms instead of La atoms enter the α -Al solution and induce a decline of d . In addition, the mixing enthalpies of Al-Fe and Al-La pairs are -11 kJ/mol and -38 kJ/mol respectively [21], indicating that it is easier to form the Al-La compound than the Al-Fe compound.

Table 2. Position 2θ and spacing d of (111) plane of α -Al in $\text{Al}_{88}\text{Fe}_6\text{La}_6$ ribbons with various circumferential speeds R_c as well as the volume fraction of amorphous phase f_a .

R_c (m/s)	$2\theta_{(111)\text{Al}}$ (deg)	d (nm)	f_a (%)
22.0 (S1)	-	-	100
14.7 (S2)	38.48	0.23376	93
11.0 (S3)	38.85	0.23162	0
7.4 (S4)	38.71	0.23242	0
Pure Al[20]	38.47	0.23381	0

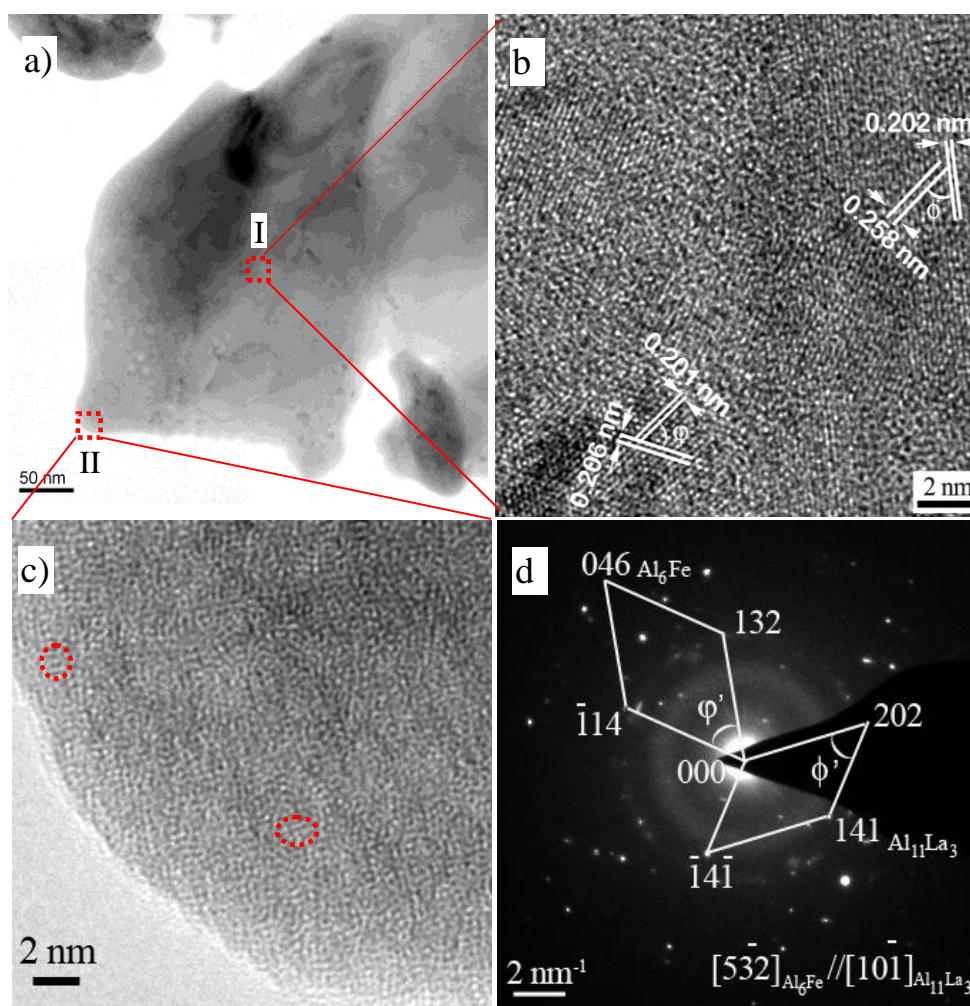


Figure 5. Structure characterization of the as-spun $\text{Al}_{88}\text{Fe}_6\text{La}_6$ ribbon with $R_c = 22.0$ m/s (S1). a) The low resolution TEM image; b) high resolution TEM image of the selected area in square I in a); c) high resolution TEM image of the selected area shown in square II in a); and d) the selected area electronic diffraction (SAED) pattern of a).

Besides the micro-scale Al-Fe and Al-La precipitates found by SEM (Fig. 4), the nano-scale details of as-spun S1 sample are characterized by low resolution transmission electron microscope (TEM) and high resolution transmission electron microscope (HRTEM), as shown in Fig. 5. From low resolution TEM image, the ribbon exhibits a heterogeneous microstructure (Fig. 5 a). The HRTEM image in selected area, i.e. square I in Fig. 5 a, shows that there exist crystalline precipitates (Fig. 5 b). The atomic lattice spacings in the right side of Fig. 5 b are 0.202 and 0.258 nm, forming an angle $\phi = 50$ deg. The atomic lattice spacings in the bottom of Fig. 5 b are 0.201 and 0.206 nm, forming an angle $\phi = 60$ deg. In the HRTEM image in selected area, i.e. square II in Fig. 5 a, there is no visible crystalline precipitate. With carefully checking, there exist 3-5 atomic size orders, as denoted by red circles, which is similar to the order found in Zr-Cu-Ni-Al bulk glass [22]. The selected area electronic diffraction (SAED) pattern for Fig. 5 a shows a typical amorphous halo (Fig. 5 d). In addition, there exist several sets of crystalline spots. One set of spots are identified as (202), (141) and (-14 -1) planes of $\text{Al}_{11}\text{La}_3$, whose spacings are 0.202, 0.255 and 0.255 nm respectively. Here the angle ϕ' between (202) and (141) planes is 50 deg, which matches the atomic image in the right side of Fig. 5 b. Another set of spots are identified as (132), (-114) and (046) planes of Al_6Fe . Moreover, the spacings of (132) and (-114) are 0.205 and 0.200 nm respectively and the angle ϕ' is 60 deg, which agrees well with the atomic image in the bottom of Fig. 5 b. These results show that there exist nano-scale $\text{Al}_{11}\text{La}_3$ and Al_6Fe in the as-spun S1 ribbon, and that the nano-scale precipitate/matrix interface is clean and in a good bonding state.

Generally, melt spinning is a rapid solidification process and atoms in the melt have little time to rearrange, resulting in the easy formation of the metastable phases [18]. Hence, it is understood the existence of the metastable Al_6Fe phase in the sample. The Al_6Fe particles are easily oxidized, forming a layer of oxide film on their surface [23,24]. In other words, the Al_6Fe phase in the ribbons is helpful to form a passive film rapidly when the ribbons are polarized in NaOH and H_2SO_4 solutions, which is also indicated by the oxygen content of the sample (Table 1).

Preliminary results [8] indicated that the addition of Fe to oxide can stabilize the Al-based oxide at high PH. According to the oxide bridging model [9], the interface between the nano-sized precipitates and amorphous matrix provides a lot of channels to transport the passivation atoms to the passive film [25,26]. Hence, the excellent passivation of Al-Fe-La alloys can be ascribed to the motion of Fe atoms to passive film through the interfaces in various scales, which is similar to the earlier results [27,28]. Meanwhile, with decreasing R_c , the size of the precipitates increases and causes a decline of total area of the precipitate/matrix interface, which weakens the oxide "bridges" and decreases the corrosion resistance of ribbons (Fig. 2).

4.2 Cracking behavior of Al-Fe-La glassy alloys

In order to further analyze the cracks in the anodic polarized samples, we pulled and broke the as-spun ribbons and took the SEM images of the cross-sections, as shown in Fig. 6. The fracture

surface of S1 has a cleavage pattern together with many fine veins. From the branching or bifurcation of the vein pattern, we can get the shear force direction (along the arrow in Fig. 6 a). Besides the vein-like fracture surface of S1 ribbon, there exists a narrow smooth region along right edge of the cross-section in width of 2.5 μm .

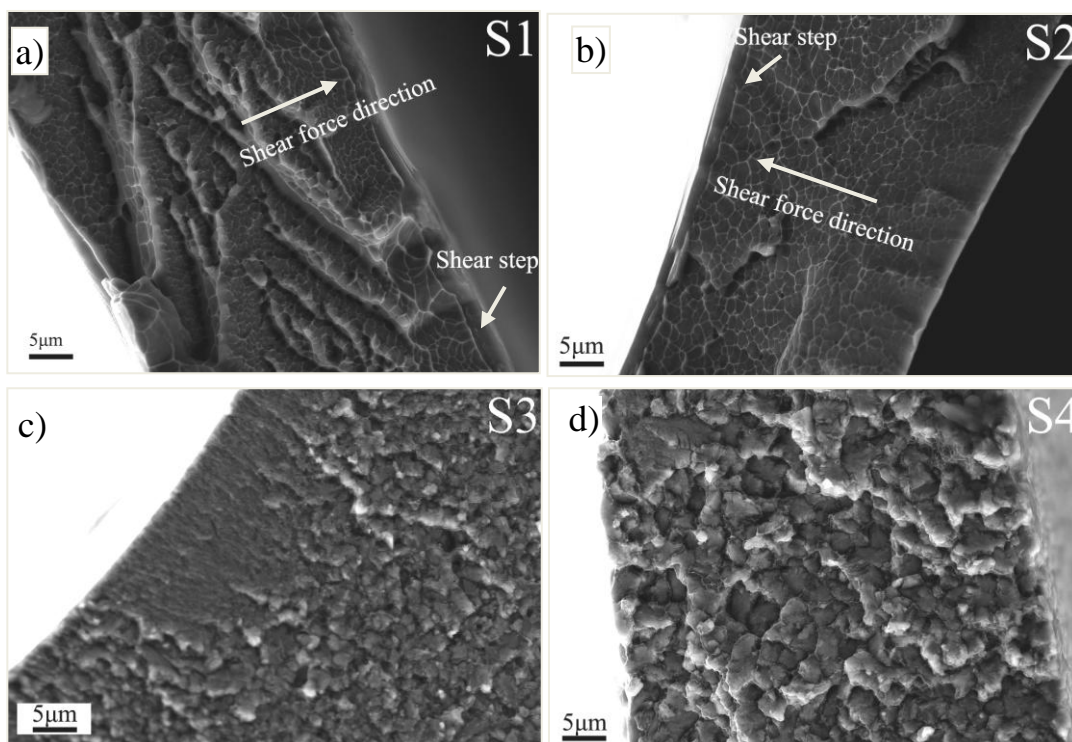


Figure 6. The SEM photographs of cross-section of the $\text{Al}_{88}\text{Fe}_6\text{La}_6$ alloys with various circumferential speeds R_c . a) $R_c = 22.0$ m/s (S1); b) $R_c = 14.7$ m/s (S2); c) $R_c = 11.0$ m/s (S3); and d) $R_c = 7.3$ m/s (S4);

The width of smooth region is considered as the displacement of shear step [29,30]. Compared with sample S1, the average area delimited by vein pattern of S2 is larger, and the shear step displacement (~ 2 μm) is a little smaller (Fig. 6 b), indicating that the ductility of S2 is a little lower. However, the fracture surface of S3 ribbon shows a cleavage patterns initiated from left edge of the cross-section, ending at 10 μm away from the edge; and the fracture surface shifts to be intergranular fracture manner, showing that the diameter of grains in the fracture surface is about 3 μm (Fig. 6 c). In sample S4, there exists only the intergranular fracture surface without the cleavage pattern and the shear step along the cross-section edges. The size of the grains in the fracture surface is about 4 μm , obviously larger than that of S3, showing a higher brittleness of S4 (Fig. 6 d). These results show that, the higher f_a a sample has, the lower brittleness it bears.

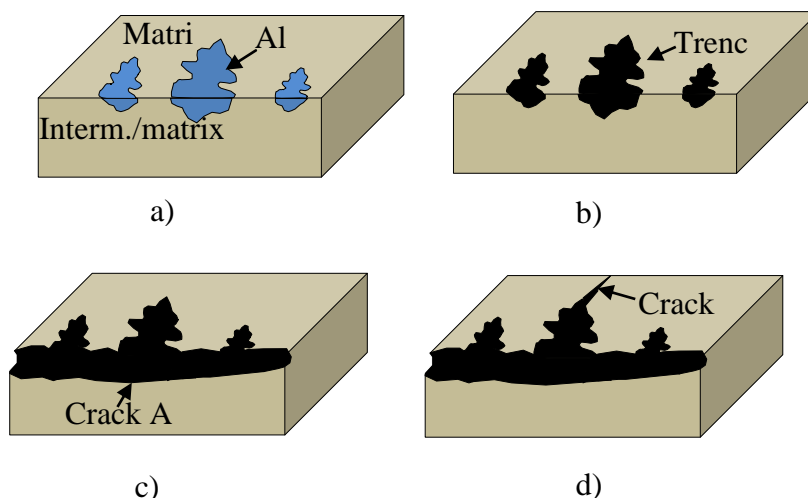


Figure 7. Formation of A and B cracks in the $\text{Al}_{88}\text{Fe}_6\text{La}_6$ ribbon. a) as-spun; b) Al phase dissolved and left trench in the matrix; c) crack A formed along the intermetallic/matrix interface; and d) crack B initiated from the edge of the trench.

On basis of above analysis, the amorphous phase has a good high ductility, the crystalline precipitates have a high brittleness. Moreover, the nano-scale interface in the sample has no deteriorating effect on the ductility, but the micro-scale interface indeed has. Hence, it is understood that crack initiates not in the internal position of the amorphous matrix, but in the micro-scale intermetallics/matrix interface (Fig. 4). The formation of cracks is schematically illustrated in Fig. 7, which will be amply explained in the following.

According to the XRD patterns and DSC curves (Fig. 1), Al phase is not the primary precipitated phase. Hence the dendritic Al phase exists in the micro-scale intermetallic/matrix interface (Figs. 6 and 9a). Here the front surface of the ribbon denotes the intermetallic/matrix interface. After the anodic polarization, the dendrite α -Al is eroded firstly for its poorer corrosion resistance (Figs. 2 and 6c and Ref. [8]), leaving the deep trenches near the intermetallic/matrix interfaces (Fig. 7 b). There exist three kinds of stresses in the as-spun samples during the anodic polarization [31,32]: residual stress, capillary forces, and coherent stress between the uncorroded and corroded parts in the sample. Under these stresses, the trenches left by dendritic Al phase can induce the cracks (A type cracks) along the intermetallic/matrix interface, thanks to its brittleness (Fig. 7 c). During the processing of the passivation, the A cracks will isolate the intermetallic precipitates from the amorphous matrix, and then the stresses are loaded on the matrix. Here, crack A can be considered as a “pit” under low stress, and we can use the novel concept of pit induced dynamic plastic strain [33], i.e., the crack initiates at the shoulder of a pit not at the pit base. Hence we can understand the crack B initiates from crack A and grows up in a direction perpendicular to crack A (Fig. 7 d). With the ongoing of corrosion, the B cracks propagate until connecting each other to form a network (Fig. 4 e). The formation of cracks is possibly helpful to obtain the glassy particles in required size, which may be useful in the powder manufacturing technology.

5. CONCLUSION

The polarization curves of Al₈₈Fe₆La₆ ribbons in NaOH and H₂SO₄ solutions show no drastic current increase up to measurement limit 10 V, indicating that the Al₈₈Fe₆La₆ alloy has a good corrosion resistance. With decreasing the circumferential speed, the corrosion resistance of Al₈₈Fe₆La₆ ribbons in NaOH and H₂SO₄ solutions decreases, too. The excellent passivation of samples can be ascribed to the heterogeneity in micro- and nano- scales (e.g. existing Al₆Fe phase, Al-La phases and 3-5 atomic layers ordered zone), which provide the easy bridges to transport the Fe atoms into the oxide film. After anodic polarization, the cracks appeared in the sample surfaces can be divided into A and B types. Crack A is the rougher, locating in the micro-scale intermetallic/matrix interfaces; crack B is linear, initiated from the sharp edge of the first type crack A. The formation of crack B is discussed based on the concept of pit induced dynamic plastic strain. The crack formation in electrolytes is possibly useful in the powder manufacturing technology.

ACKNOWLEDGMENTS

The authors acknowledge the National Natural Science Foundation (No.51171091), the Excellent Youth Project of Shandong Natural Science Foundation (JQ201012), the National Basic Research Program of China (973 Program) (2012CB825702) for financial supports.

References

1. B.P. Zhang, A. Kawashima, H. Habazaki, K. Asami, K. Hashimoto, *Corros. Sci.*, 39(1997) 2005-2018.
2. M.A. Jakab, J.R. Scully, *Nature Mater.*, 4(2005) 667-670.
3. L. Li, Q. Qu, Z.W. Fang, L. Wang, Y.W. He, R. Yuan, Z.T. Ding, *Int. J. Electrochem. Sci.*, 7(2012) 12690-12705.
4. R. Li, W.M. Wang, H.J. Ma, G.H. Li, J.Y. Qin, Z.H. Zhang, X.W. Tang, *Trans. Nonferrous Met. Soc. China*, 21(2011) 81-87.
5. X.Q. Wu, C.Q. Xie, *J. Rare Earths*, 26(2008) 745.
6. M.G. Alvarez, S.M. Vazquez, F. Audebert, H. Sirkin, *Scripta Mater.*, 39(1998) 661.
7. C.A.C. Sousa, C.S. Kiminami, *J. Non-Cryst. Solids*, 219(1997) 155.
8. A.M. Lucente, J.R. Scully, *Corros. Sci.*, 49(2007) 2351-2361.
9. M. Mehmood, B.P. Zhang, E. Akiyama, H. Habazaki, A. Kawashima, K. Asami, K. Hashimoto, *Corros. Sci.*, 40(1998) 1-17.
10. Z.Z. Yuan, X.D. Chena, B.X. Wang, *J. Mater. Sci.*, 41(2006) 3481-3487.
11. L.C. Zhuo, S.J. Pang, H. Wang, T. Zhang, *J. Alloys Compd.*, 504(2010) s117-s122.
12. J.K. Zhou, X.F. Bian, W.M. Wang, X.Y. Xue, S.H. Wang, Y. Zhao, K.B. Yin, *Mater. Lett.* 58(2004) 2559.
13. G.H. Li, Study on glass forming ability, *Crystallization and properties of Al-TM-RE based amorphous alloys*, Dissertation, Shandong University, 2010.
14. K. Mondal, B.S. Murty, U.K. Chatterjee, *Corros. Sci.*, 47(2005) 2619-2635.
15. H.J. Ma, W.M. Wang, J. Zhang, G.H. Li, C.D. Cao, H.D. Zhang, *J. Mater. Sci. Tech.*, 2011(27) 1169-1177.

16. A. Gebert, V. Haehnel, E.S. Park, D.H. Kim, L. Schultz, *Electrochim. Acta*, 53 (2008) 3403–3411
17. W.B. Liu, S.C. Zhang, N. Li, J.W. Zheng, S.S. An, G.X. Li, *Int. J. Electrochem. Sci.*, 7 (2012) 7993 – 8006.
18. F. Kurz, *Fundamentals of Solidification*, Trans Tech Public, 1992, Switzerland.
19. Y. Zhou, G.H. Wu, *Materials Analysis and Testing Technology*, Harbin Institute of Technology Press, 1998, Harbin.
20. *PCPDFWIN*, Version 2.02, (International Center for Diffraction Data, 2002).
21. A. Takeuchi, A. Inoue, *Mater. Trans.*, 12(2005) 2817-2829.
22. J. Das, M.B. Tang, K.B. Kim, R. Theissmann, F. Baier, W.H. Wang, J. Eckert, *Phys. Rev. Lett.*, 94(2005) 205501.
23. C.A. Aliravci, M.Ö. Pekkülyüz, *Calphad*, 22(1998) 147-155.
24. K. Shimizu, G.M. Brown, H. Habazaki, K. Kobayashi, P. Skeldon, G.E. Thompson, G.C. Wood, *Corros. Sci.*, 41(1999) 1783-1790.
25. C.A.C. Souza, F.S. Politi, C.S. Kiminami, *Scripta Mater.*, 39(1998) 329-334.
26. D. Szewieczek, J. Tyrlik-Held, Z. Paszenda, *J. Mater. Process. Technol.*, 78(1998) 171-178.
27. H. Alves, M.G. S. Ferreira, U. Koester, *Corros. Sci.*, 45(2003) 1833-1845.
28. C.G. Tan, W.J. Jiang, Z.C. Zhang, X.Q. Wu, J.G. Jin, *Mater. Chem. Phys.*, 108(2008) 29-34.
29. F.E. Luborsky, *Amorphous Metallic Alloys*, Butter Worth, London, 1983.
30. J.M. Park, G. Wang, R. Li, N. Mattern, J. Eckert, D.H. Kim, *Appl. Phys. Lett.*, 96(2010) 031905.
31. J.R. Hayes, A.M. Hodge, J. Biener, A.V. Hamza, K.J. Siczadzki, *J. Mater. Res.*, 21(2006) 2611.
32. X.G. Wang, Z. Qi, C.C. Zhao, W.M. Wang, Z.H. Zhang, *J. Phys. Chem. C*, 113(2009) 13139.
33. A. Turnbull, L. Wright, L. Crocker, *Corros. Sci.*, 52(2010) 1492-1498.